JOURNAL OF SPACECRAFT AND ROCKETS
Vol. 40, No. 5, September–October 2003

Novel Approach for Maneuvering Reentry Vehicle Design

T. C. Lin,* L. K. Sproul,* S. A. McKeel,* and T. P. Shivananda*
TRW Systems, San Bernardino, California 92402
and
J. Kealos,* P. Fote,† N. Thyson,‡ and B. L. Reeves*
Textron Systems, Wilmington, Massachusetts 01864

A novel approach to the design of a trajectory-shaping reentry vehicle is proposed. The design takes advantage of readily available aeroshells and control devices. The idea is to use existing hardware with minimal changes to the substructure to perform the maneuvering mission at a minimum cost. Most of the new hardware required to perform the maneuvering flight is available as commercial-off-the-shelf items. One distinguishing feature of the present design is that the basic aerodynamics of the reentry vehicle are not affected by the control devices during the lifting maneuvers. The fuel required to conduct the glide/evasion is kept to a minimum; at the same time the reentry vehicle can attain large angle of attack if needed. The basic concept of the approach is 1) to place the reentry vehicle center of mass at the aerodynamic center and 2) to insert four to six reaction jets at the reentry vehicle base as close to the centerline as possible. Wind-tunnel tests and numerical computations were performed to substantiate the present design.

Nomenclature

A	=	reference area
$ALPP$	=	angle of attack, deg
$C_{N\alpha}$	=	slope of normal force coefficient
d	=	jet nozzle throat diameter
F_{jet}	=	jet thrust force
h	=	altitude or distance from nozzle exit to Mach disk
L	=	total body length
ℓ	=	distance between base-mounted jet and missile/reentry-vehicle center of gravity
M_e	=	Mach number at the boundary-layer edge
M_∞	=	freestream Mach number
p_{ambient}	=	ambient pressure or reference pressure
p_{flare}	=	static pressure on the flare
p_{wall}	=	surface pressure
p_0, p_{0c}	=	jet stagnation pressure
p_{0e}	=	stagnation pressure in the shock layer at the edge of the boundary layer
q_∞	=	freestream dynamic pressure
Re	=	freestream Reynolds number per foot
r_B	=	body base radius
r_C	=	body cylinder radius
SM	=	static margin, $X_{\text{cp}} - X_{\text{CG}}$
TT	=	freestream total temperature
X_{CG}	=	axial distance measured from nose stagnation point to reentry vehicle's center of mass
X_{cp}	=	axial distance from nose stagnation point to reentry vehicle's center of pressure
x	=	axial distance
γ_e	=	specific heat ratio of shock-layer gas
γ_j	=	specific heat ratio of injected gas
θ	=	cone half-angle, deg

Received 28 May 2002; revision received 3 January 2003; accepted for publication 6 January 2003.

*Member of Technical Staff, Missile Defense Division. Member AIAA.
†Program Manager, Missile Systems.
‡Director, Missile Systems. Member AIAA.

Introduction

THERE are many existing control concepts that can be used in designing a trajectory-shaping reentry vehicle (TsRV), for example, variable flare geometries, multiflaps/split windward flaps, aileron/fin devices, swivel nose/radial moving mass, and frustum-mounted jets. All of these TsRV designs have their advantages and disadvantages. One of the disadvantages shared by all of these concepts is that the basic bare-body aerodynamic coefficients are affected by the addition of the control devices.

Figure 1 illustrates the flowfield around a frustum-mounted jet. The jets have the potential to induce boundary-layer separation, strong viscous flow, and shock-layer interaction. The viscous interactions are strongly affected by the state of the boundary-layer flow, that is, whether it is laminar, transitional, or turbulent. Separated flow can increase local heating, creating an issue for the thermal protection design, and ultimately an increase in reentry vehicle (RV) weight.

One disadvantage of frustum-mounted jets or multiflaps is that the flowfield can be inherently unsteady if the boundary layer is separated. The aerodynamic coefficients can be difficult to predict because they depend highly on the Reynolds and Mach numbers. Extensive wind-tunnel tests are required to nail down the basic trim aerodynamics. In most cases ground-test facilities cannot duplicate the flight environments (e.g., the Reynolds-number and Mach-number similitude, etc). Consequently, only expensive and time-consuming flight tests can truly validate the aerodynamics.

A new design approach is presented in this paper, which employs a different control mechanism. The salient features of the presented design are that it can use existing hardware such as the aeroshell and control devices. The control devices are available as commercial-off-the-shelf items. Wind-tunnel testing can be kept to a minimum because the aerodynamic coefficients are well known for the simple conic bodies. Finally, the fuel required to perform the maneuvering mission (e.g., large angle of attack or long lifting flight time) can be kept to a minimum. This is possible because the aerodynamic uncertainties are small, and only small control forces are needed to perform large angle-of-attack maneuvers.

Basic Design

The basic design employs an axial moving mass to place the TsRV center of gravity (X_{CG}) at its center of pressure (X_{cp}) position.[1] Figure 2 illustrates the present design approach. Under this arrangement the TsRV static margin can be maintained at almost zero value. Four jet reaction controls (JRC) are placed at the base of the TsRV to induce the necessary trim force to perform lifting flight. Two

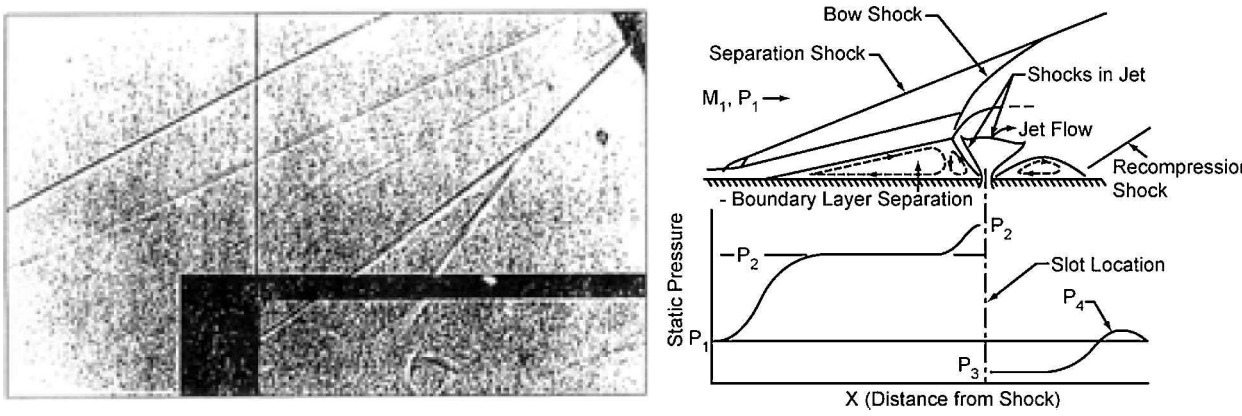

Fig. 1 Environmental shadowgraph of a typical jet interaction and sketch of flowfields and pressure distribution (frustum-mounted jet).

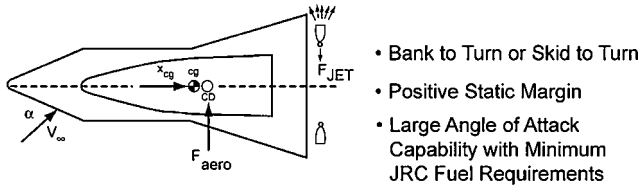

a)

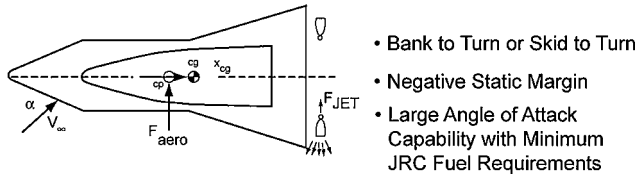

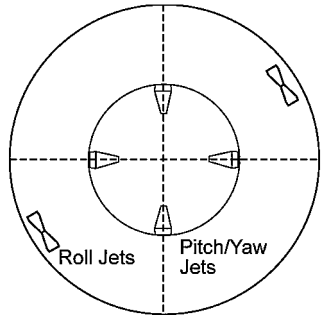

b)

Fig. 2 New control concepts for maneuvering vehicle design: a) $SM > 0$ and b) $SM < 0$.

additional control jets are placed on the TsRV base to control roll position.

With this arrangement, it is possible to obtain a large angle of attack with very small jet thrust, that is,

$$\alpha = \frac{\kappa F_{\text{jet}} \ell}{C_{N_\alpha} q_\infty A(SM)} \tag{1}$$

where α is the desired angle of attack, $\ell = L - X_{\text{CG}}$, and κ the amplification factor.

As the static margin approaches zero by the proper actuation of the axial moving mass (i.e., $SM \to 0$), the required JRC thrust can become very small, $F_{\text{jet}} \to 0$. In fact, very large angle of attack α can be achieved even with small JRC thrust. Therefore, one can minimize JRC fuel consumption or RV weight. In principle, the JRC can be fired for jets located on the leeward plane when the static margin is positive ($SM > 0$; Fig. 2a) or for jets located near the windward plane when the static margin is negative ($SM < 0$; Fig. 2b). The advantage and disadvantage of these two approaches will be discussed later.

The TsRV aeroshell can be any existing conic or biconic body with sufficient payload capabilities. It is particularly attractive to use decommissioned reentry vehicles because their basic aerodynamic coefficients are known through flight experience. The hardware for JRC control can be purchased as commercial-off-the-shelf items. The design and manufacture of the axial moving mass is not a trivial task. The hardware must withstand the maneuvering axial and lateral loads during ascent and reentry flight, and it must actuate fast enough to perform the desired command. But the task is straightforward. A prototype of axial moving mass hardware design has been demonstrated by Textron.[1]

It must be emphasized that the present approach can be applied to any aerodynamic frame, regardless of its lift-to-drag (L/D) ratio or range of flight Mach-number regime. The body cross section does not have to be circular or axisymmetric. The control algorithms can be skid-to-turn or bank-to-turn. Another important advantage of the proposed design is its fast lifting force reaction time because TsRV static margin can be made as small as the design allows.

Concept Validation

One of the important requirements for the proposed design is that excursions of the center of pressure during flight in response to control commands must be well behaved in order to easily keep $X_{\text{CG}} \approx X_{\text{CP}}$. In other words, the RV c.p. position should be a known function of Mach number, Reynolds number, and angle of attack. It should not be strongly affected by the Reynolds number or boundary-layer transition phenomena. More importantly, shock-layer flow separation should be avoided, if possible. This requirement can be met by locating the jet nozzles at the TsRV base and recessing them below the base shoulder, so that the penetration of the jet plume will not affect the RV frustum shock layer. An engineering criterion is proposed herein to provide guidelines on positioning the base-mounted jets. First, we shall define the flow regimes and then delineate the rationale for specifying the optimum JRC locations.

Three primary flow regimes have been identified for the baseline design thruster location. These flow regimes, and the methodology used to compute the plume Mach disk location and the plume penetration height into the shock layer, are delineated as follows.

Regime 1

The Mach disk is located within the base recirculation region (Fig. 3).

Table 1 Leeward meridian Mach disk location and penetration height for flight conditions (R_B = RV base radius = 15.8 in., d = 1.03 in., p_{0j} = 400psi)

Altitude, kft	M	α	Me	P_{flare}, psi	$h^{(1)}$ ($P_a = P_{\text{base}}$), in.	$h^{(2)}$ ($P_a = P_{\text{flare}}$), in.	$h^{(3)}$, in.
72	19.0	4.7	4.75	6.770	17.22	5.11	1.86
66	20.9	1.6	5.00	18.48	15.00	3.10	1.02
43	13.2	9.9	4.70	3.130	8.700	7.50	2.90
34	12.7	7.6	4.54	13.90	7.00	3.60	1.32

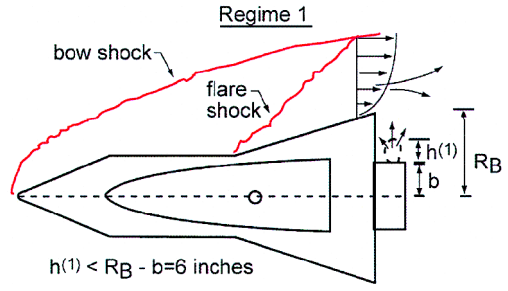

Fig. 3 Regime 1.

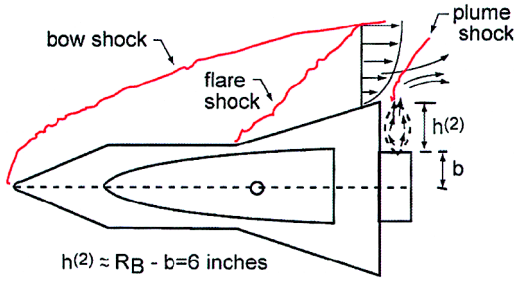

Fig. 4 Regime 2.

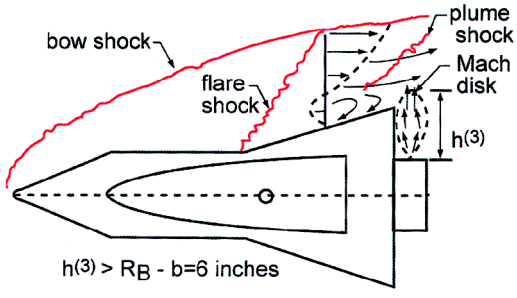

Fig. 5 Regime 3.

The position of the Mach disk can be approximately estimated from the Crist et al. correlation[2] for a jet exhausting into a quiescent gas, that is,

$$h/d = 0.645(p_0/p_{\text{ambient}})^{0.5} \tag{2}$$

In this flow regime p_{ambient} is taken to be the base pressure, and we estimate it to be roughly equal to p_∞, depending on the jet injection rate. This approximation ($p_{\text{base}} \approx p_\infty$) appears to be supported by wind-tunnel tests, as will be discussed later.

Regime 2

The Mach disk is located near the RV base shoulder (Fig. 4). There is significant lateral deflection of the base-flow separated shear layer but negligible flow interference with the flow in the frustum shock layer. In this flow regime the Mach disk location can be approximately estimated from Eq. (2) with $p_{\text{ambient}} = p_{\text{flare}}$, where p_{flare} is the undisturbed RV frustum pressure.

Regime 3

The Mach disk is located well above the RV shoulder region and starts to perturb the frustum shock layer (Fig. 5). Flow separation upstream of the plume causes higher pressure on the frustum and significant flow interference. The penetration height measured from the nozzle exit can be approximately estimated from the Zukoski and Spaid correlation[3,4] for lateral injection into a supersonic/hypersonic shock layer. The correlation yields

$$\frac{h_3}{d} = \frac{1}{M_e}\left(\frac{p_0}{p_e}\frac{\gamma_j}{\gamma_e}\frac{2}{B}\right)^{\frac{1}{2}} E \tag{3}$$

$$B = \frac{2}{\gamma_e M_e^2}\left\{\left[\frac{(\gamma_e+1)M_e^2}{2}\right]^{[\gamma_e/(\gamma_e-1)]}\left[\frac{\gamma_e+1}{2\gamma_e M_e^2 - \gamma_e + 1}\right]^{1/(\gamma_e-1)} - 1\right\}$$

$$E = \left\{\left(\frac{2}{\gamma_j-1}\right)\left(\frac{2}{\gamma_j+1}\right)^{[(\gamma_j+1)/(\gamma_j-1)]}\left[1-\left(\frac{p_e}{p_0}\right)^{(\gamma_j-1)/\gamma_j}\right]\right\}^{\frac{1}{4}}$$

where M_e is the Mach number at the boundary layer edge in the meridian plane of the thruster and p_e is the flare pressure at the base shoulder in the meridian plane of the thruster (i.e., $p_e = p_{\text{flare}}$).

The procedure used to compute the baseline design Mach disk location and jet penetration height at various trajectory points is as follows: At each critical flight condition plume penetration heights are first computed using the regime 1 correlation [Eq. (2)]. When the computed penetration height is bigger than the nozzle exit offset distance below the RV's shoulder, the Mach disk position is computed using regime 2 and regime 3 correlations. If the penetration height is less than the nozzle offset distance, there is no jet-interaction plume perturbation on the reentry vehicle forebody aerodynamics. The only perturbation is the slight axial-force coefficient reduction produced by nozzle plume impingement on the base.

Table 1 illustrates the procedure used to estimate the Mach disk location. In this example, the jet stagnation pressure is $p_{0c} \sim 400$psi, and $\gamma_j = 1.2$. For all cases considered, the inviscid shock-layer properties M_e and p_e were evaluated at the RV aft station using Hall and Sontowski's three-dimensional inviscid flow finite difference code.[5] The thruster is located on the leeward meridian because the surface pressure is lowest at the leeward meridian and the penetration height is largest.

For the example considered in Table 1, the nozzle exit is recessed 6 in. below the shoulder of the RV base. The location of the Mach disk $h^{(1)}$, or the penetration height into the leeward shock layer, is first computed using Eq. (2) with $p_b \approx p_\infty$ in Table 1. Everywhere $h^{(1)}$ is greater than the nozzle offset distance of 6 in. With $h^{(1)} > 6$ in., it is possible to test on values of $h^{(2)}$ and $h^{(3)}$. If $h^{(2)}$ is less than 6 in., then there is no penetration into the frustum shock layer, and the Mach disk is predicted to be located at the base shoulder with the pressure downstream of the disk at the same level between p_e and p_B. This criterion is met by all cases considered in Table 1 except at 43 kft altitude (where $h^{(2)} = 7.5$ in. > 6.0 in.). Some degree of shock penetration is predicted for this case. Examination of values of $h^{(3)}$ from the Zukoski–Spaid correlation shows that $h^{(3)}$ is less than 6 in. for all of the flight conditions considered in Table 1, so that no significant shock-layer penetration is predicted using Eq. (3). For the case of $h^{(2)} > 6$ in. (and $h^{(3)} < 6$ in.), the Mach disk probably extends past the shoulder somewhat, with p_{ambient} slightly greater

than p_e, but with insufficient shock-layer penetration to produce a strong normal shock upstream of the plume. In the event that the calculated $h^{(3)}$ is larger than the nozzle offset distance, one can either lower the jet chamber pressure, move the nozzle inward, or fire the jet at the windward meridian. The empirical correlations defining the three flow regimes will be checked with the wind-tunnel tests, as discussed later.

The selection of nozzle exit position is important because it can minimize the aerodynamic uncertainties as compared to the case of frustum-mounted JRC. Additionally, the aerodynamic coefficients of the RV are unaltered from the original reentry body's aerodynamics. Therefore, no new wind-tunnel tests are required to define the TsRV aerodynamics as would be needed for TsRV with flaps, fins, frustum-mounted jets, or bent cone.

Numerical Simulations

To validate our design concepts, wind-tunnel tests and computational fluid dynamics (CFD) were performed. Three-dimensional inviscid flow,[5] parabolized Navier–Stokes, and Navier–Stokes formulation [e.g., Generalized Aerodynamic Simulation Program (GASP)[6] and Advanced Aerothermal Algorithm (AAA)[7] codes] were used to estimate the complex flowfields for a RV at angle of attack with base-mounted jets located at the leeward and windward planes. Both laminar and turbulent flow with equilibrium air conditions were calculated.

For the GASP code the numerical grid was constructed with GRIDGEN and six zones; 467,154 cells were used in most of the calculations reported here. Grid refinements with 1.5×10^6 and 930,300 cells were carried out at 9-deg angle of attack and hypersonic flow to ascertain the numerical convergence. The three sets of grid systems gave comparable results.

For wind-tunnel simulations, no slip, constant surface temperature, and no wall ablation boundary conditions were specified. The jets were simulated by specifying a 10-deg divergent nozzle exit condition. The Baldwin and Lomax algebraic turbulence model was used in most of the numerical computations, although the two-equation k–ε turbulence model was also used to compare with the turbulent algebraic model results. The numerical results of the CFD code were also validated with wind tunnel data as will be shown later.

Data on a sphere-cone-cylinder-flare (SCCF) body geometry are presented here to illustrate the new design approach. The configuration is shown in Fig. 6a ($r_B = 15.9$ in., $r_C = 9.5$ in., $\theta_1 =$ fore cone angle $= 20$ deg, $\theta_2 = 0$ deg, and $\theta_3 =$ flare angle $= 15$ deg).

Figure 6b depicts the pressure contours (isobar) on the SCCF at 80 kft altitude with the JRC firing in the base region. The freestream Mach number is 22, and the angle of attack is zero. The corresponding velocity vector projection is shown in Fig. 7. The numerical results indicate no jet plume penetration into the flare region. Figure 8 depicts the surface-pressure distribution on the vehicle surface. It shows that the wall pressure is the same, with or without the base-mounted jets. The interaction of the plume Mach disk and the hypersonic shock layer takes place away from the body, where the pressure can be very high as shown in Fig. 6.

Results at 10-deg angle of attack and altitude 80 kft are given in Figs. 9–11. Herein, the JRC is located at the leeward meridian. At this high altitude and relatively large angle of attack, the leeward flowfields start to be affected by the Mach disk penetration. Figure 10 shows that the boundary layer in the rear flare region is separated at the leeward plane. The adverse pressure gradient, observed along the leeward meridian, is another indication of upstream influence by the JRC plume (Fig. 11). Consequently, the basic aerodynamics of the trajectory-shaping vehicle could be affected by the flow separation. One way to obtain high angle of attack without the jet interference is to place the jets at the RV base on the windward plane, and move the c.g. slightly behind the c.p. (i.e., $SM < 0$; see Fig. 2b). In this way, according to our CFD results, no boundary-layer separation would occur, even at 20-deg angle of attack and at altitude of 80 kft.

Wind-Tunnel Tests

The CFD computations were compared with wind-tunnel tests,[8] which were conducted at Arnold Engineering Development Center (AEDC) in Tullahoma, Tennessee, in May 1999. Tests were run in Tunnel B at Mach 8 and Tunnel A at Mach 4 conditions. Both laminar and tripped turbulent flow conditions were employed. Several boundary-layer trip heights varying from 10 to 100 mils were explored. Most of the measurements were conducted with boundary trip height of 78 mils located aft of the nose-tip region.

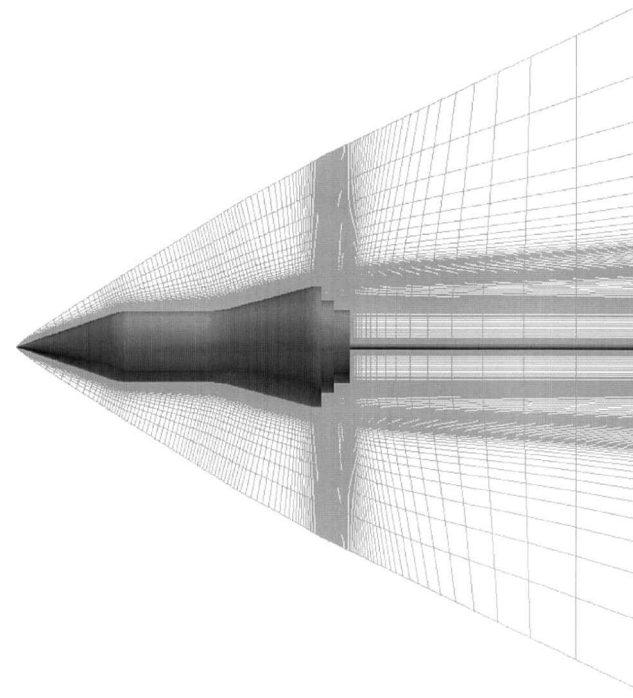

Fig. 6a Representative numerical grids used in the CFD calculations.

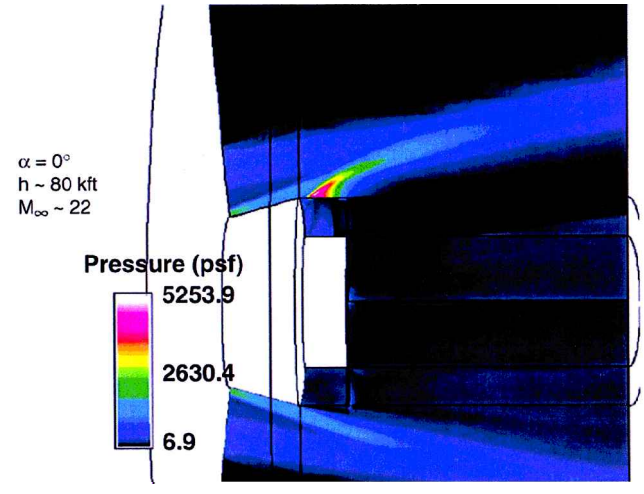

Fig. 6b Pressure contour near reentry vehicle base region ($\alpha = 0$ deg).

The test model was a 40% subscale configuration of a representative reentry vehicle (i.e., a multiconic body with base radius of $r_B = 15.9 \times 0.4 = 6.36$ in.; Figs. 12a and 12b). The base-mounted jets were arranged in several locations (Fig. 12c) below the base shoulder to test the engineering relations [i.e., Equations (2) and (3)] for Mach disk location.

The test measurements consisted of force and moment, surface pressure, heat transfer, and flow visualization. The high-quality shadowgraph images can show details of thruster plume-shock-layer interaction, embedded shocks, and, in some cases, flow separation. One representative example is shown in Fig. 12d, which reveals a complex flow pattern near the RV base region with plume-shock layer interaction.

Wind-tunnel conditions were carefully selected to achieve similitude of jet plume interaction effects in the ground-test facility. This

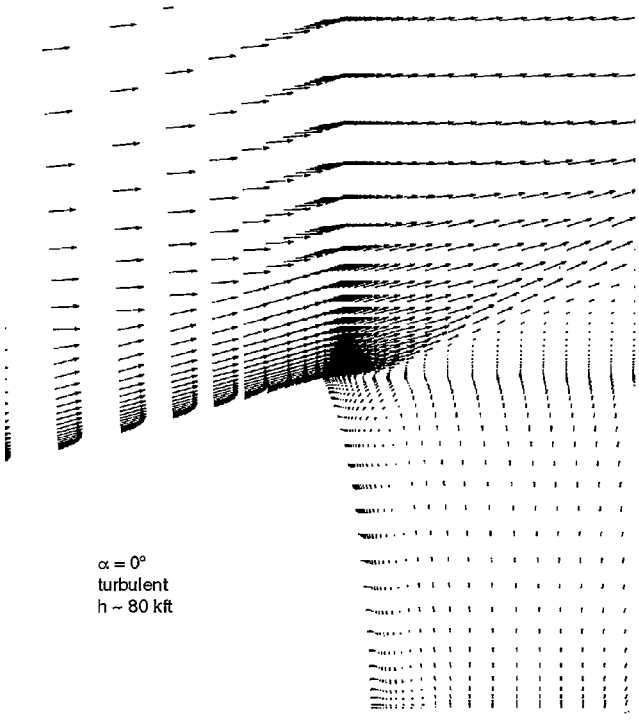

Fig. 7 Velocity vector projection near the RV base at h = 80 kft and α = 0 deg, showing no frustum boundary-layer separation.

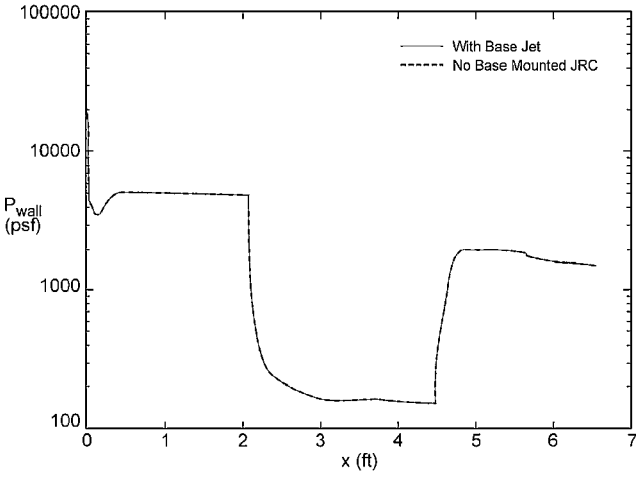

Fig. 8 RV surface pressure at h = 80 kft and α = 0 deg, showing no influence of base-mounted jet upon the wall pressure.

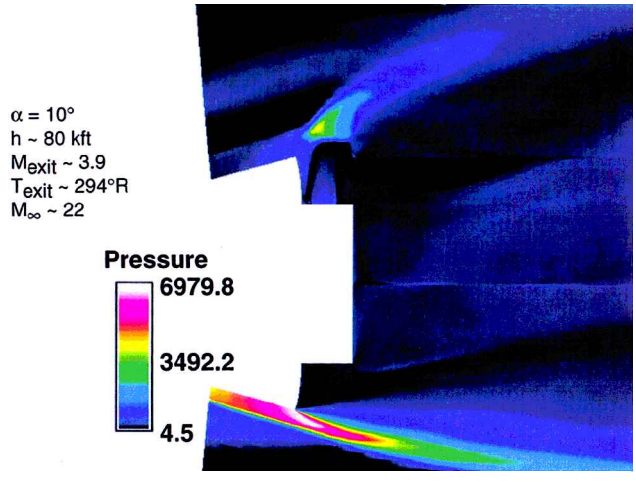

Fig. 9 Pressure contour near reentry vehicle base region (α = 10 deg).

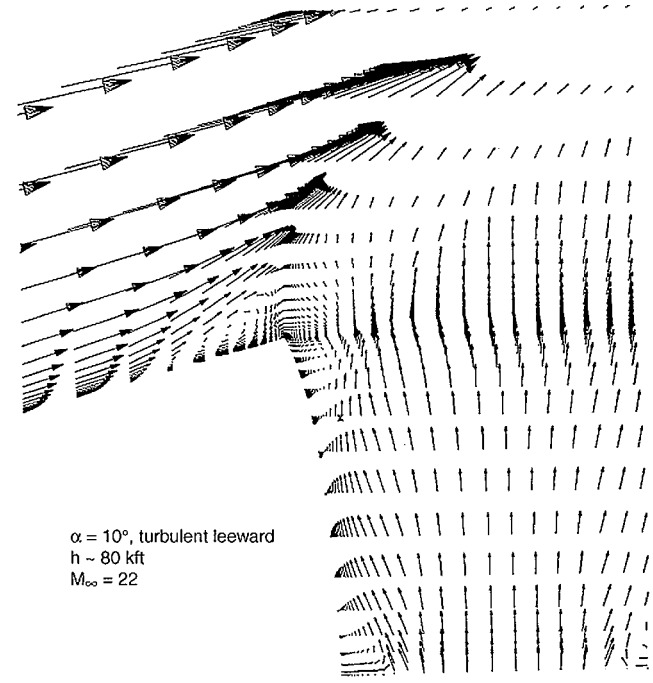

Fig. 10 Velocity vector projection near the leeward plane at α = 10 deg. (Boundary layer is separated near the end of leeward flare.)

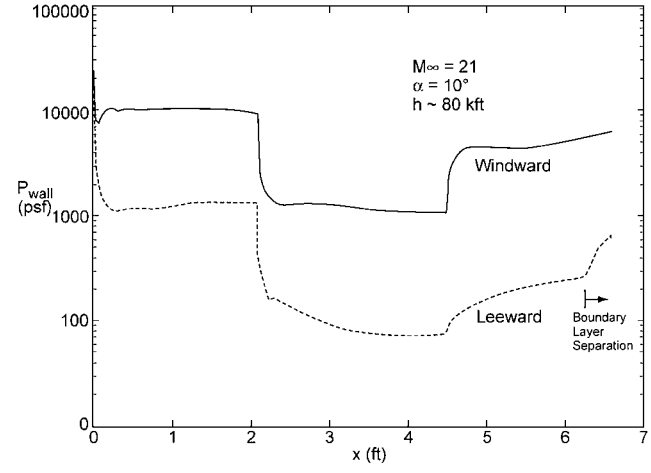

Fig. 11 Surface-pressure distribution at α = 10 deg and h = 80 kft, showing JRC interference and leeward boundary-layer separation.

requires the replication of the ratio of p_{0c}/p_{0e}:

$$(p_{0c}/p_{0e})_{\text{flight}} = (p_{0c}/p_{0e})_{\text{wind-tunnel}}$$

This ratio was varied over a large range in the test program, covering altitudes from sea level to over 120 kft. This experiment thus provides an extensive aerodynamic interaction database for vehicle angles of attack from +9 (windward thrusters) to −12 deg (leeward thrusters). Several nozzle designs/positions were tested. Tests were performed for single and dual pitch/yaw thrusters, and with a single pitch thruster operating with a roll control thruster.

Air was used as the injected gas. In flight $\gamma_j = 1.2$, whereas in the tunnel tests $\gamma_j = 1.4$. Based on the Zukoski–Spaid correlation, for a given pressure ratio, the penetration height in the tunnel tests is larger than in flight by the ratio $(1.4/1.2)^{1/2} = 1.08$.

The experimental measurement uncertainties at AEDC Tunnels A and B are given as follows: the surface-pressure gauge will give a 5.2% accuracy on the readings in the range of measurement interest. For heat-transfer rate data, the quoted uncertainties are 5% in the nominal range of 0.5 to 10 Btu/(ft^2 s). There were many repeated runs to establish data repeatability. The uncertainties on

Table 2 Mach disk location and plume penetration heights for AEDC wind-tunnel conditions (p_∞ = 0.071 psia)

M_∞	α	p_e, psia	M_e	p_{0c}, psia	$h^{(1)}$	$h^{(2)}$	$h^{(3)}$	Comments
8	0	0.46	2.81	60	7.5	2.95	1.841	No jet interference ($h < 2.4$ in.)
8	6 (lee)	0.22	3.256	60	7.5	4.26	2.32	No jet interference ($h < 2.4$ in.)
8	6 (wind)	0.903	2.435	60	7.5	2.1	1.50	No jet interference ($h < 2.4$ in.)
8	9 (lee)	0.157	3.44	60	7.5	5.0	2.61	Jet interference ($h > 2.4$ in.)
8	9 (wind)	1.235	2.257	60	7.5	1.80	1.38	No jet interference ($h < 2.4$ in.)

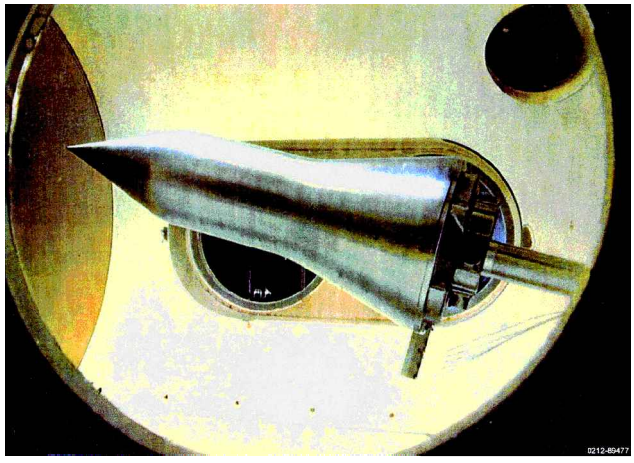

Fig. 12a AEDC Wind-Tunnel model configuration (r_B = 6.36 in., θ_1 = 20 deg, θ_2 = 0 deg, θ_3 = 15 deg).

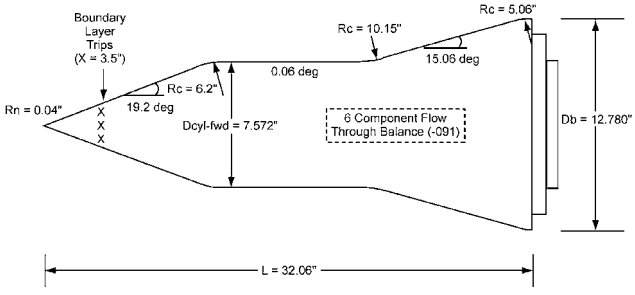

Fig. 12b Wind-tunnel test model (40% subscale configuration).

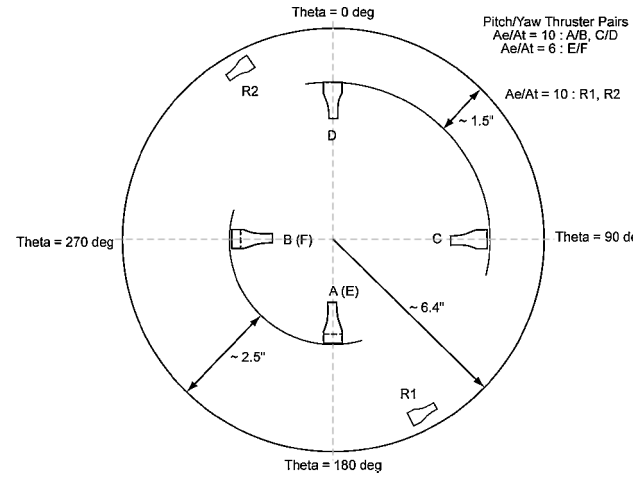

Fig. 12c Aft view of model base: thruster locations.

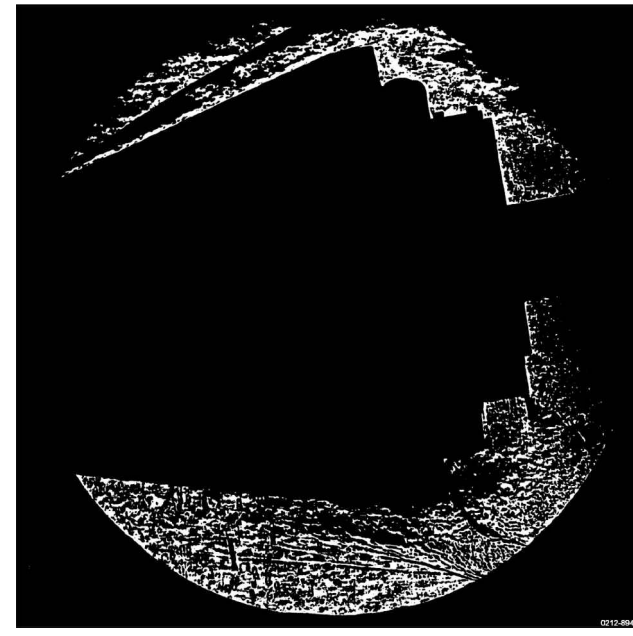

Fig. 12d Tunnel B test shadowgraphs: $M\infty$ = 8, α = −9 deg, jet "A", and p_{0c} = 120 psi.

the freestream parameters are Mach number 8 ± 0.03 at Tunnel B and 4 ± 0.02 at Tunnel A and Reynolds number 3.0E + 6 ± 3.3E + 4 at Tunnel B. The accuracy on force and moment coefficient measurements is 3 and 5% of the maximum measured values, respectively.

First, the estimate of Mach disk location for a base-mounted jet was validated. Table 2 depicts the computations of Mach disk heights $h^{(1)}$, $h^{(2)}$, and $h^{(3)}$ for AEDC Tunnel B ($M_\infty \sim 8$) as discussed earlier [e.g., Eqs. (2) and (3)]. The numerical results in Table 2 indicate that there is no plume interference on the frustum flowfield except at a leeward plane at angle of attack of $\alpha = 9$ deg (with the jet firing toward the leeward side). The AEDC Tunnel B wall pressure and schlieren photograph observations discussed in the following paragraphs appear to correlate with the approximate empirical correlation. This indicates that Eqs. (2) and (3) can be used to place the base-mounted jets in order to avoid JRC flow interference.

Figure 13a depicts the Tunnel B, Mach 8 measured surface-pressure distribution at the leeward plane at zero angle of attack with various jet stagnation pressures (i.e., $p_{0c} = 0$ to 277 psia). Under all conditions the frustum pressure is not affected by the operations of the JRC even at the highest $p_{0c} = 277$ psia. Comparing the wind-tunnel data with predicted wall pressure without jet injection indicates that JRC operation does not affect basic TsRV aerodynamics. Tunnel B results are similar for jet operation at the leeward plane at $\alpha = 6$-deg angle of attack (Fig. 13b). Again, there is no jet plume interference on the frustum flowfields for all jet stagnation pressures considered in the AEDC Tunnel B test matrix except at the highest jet stagnation pressure $p_{0c} = 278$ psia.

Jet interaction effects were also considered for angle of attack of 9 deg, with the jets fired at either the windward or leeward plane. Those tests showed that frustum surface pressure is not affected on either the windward or leeward side by jet operation in the base region for windward thrust at $\alpha = 9$ deg (Figs. 14a and 14b) at all jet stagnation pressure values p_{0c} considered in the AEDC Tunnel B experimental matrix. On the other hand, the surface pressure on the leeward plane was altered by leeward thrust at $\alpha = -9$ deg and JRC chamber pressure $p_{0c} > 119$ psi (Fig. 14d). The perturbations

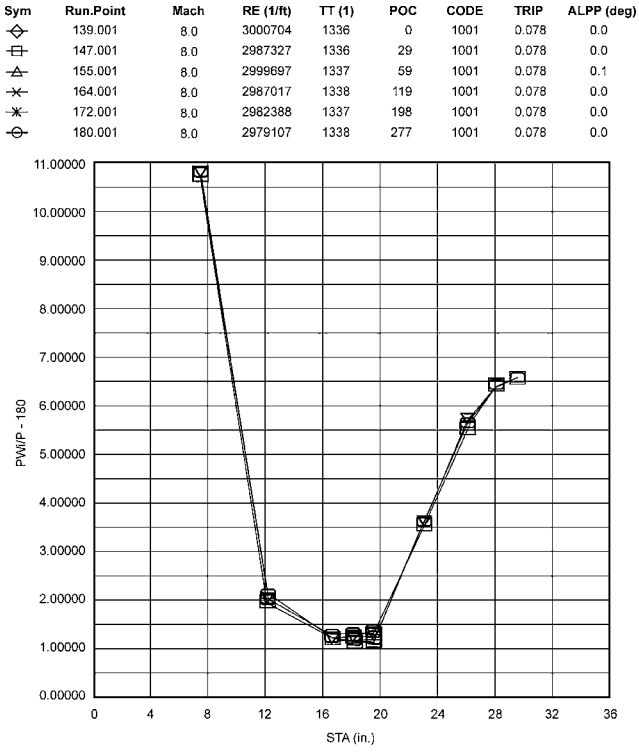

Fig. 13a Wind Tunnel B surface-pressure distributions: α = 0 deg. (Reaction jets are fired at the model base.)

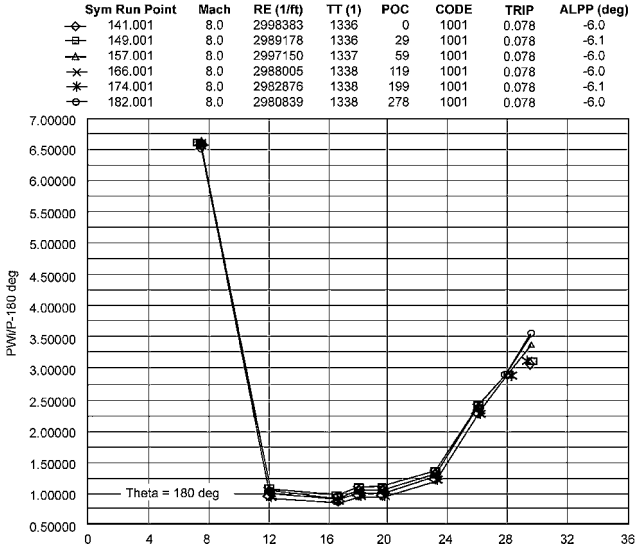

Fig. 13b AEDC Wind Tunnel B surface-pressure distributions (non-dimensionalized with freestream pressure) with leeward jet at α = 6 deg.

from the base plume are large enough to cause leeward boundary layer separation. The separation bubble penetrates ahead of the flare section and extends as far forward as the cylindrical section of the body. When this occurs, the basic TsRV's aerodynamics are affected by the operations of base-mounted jets. As mentioned before, the flow separation can be avoided by implementing the thrust at the windward meridian. The windward thrust represents the case at which the TsRV would operate at a negative static margin (Fig. 2b).

Figures 15a and 15b present AEDC Tunnel B measured force and moment coefficient data derived from Tunnel B's six-component flow-through balance. The figures show body-fixed aerodynamic coefficients with and without the base-mounted jet as a function of angle of attack. The freestream Mach number is eight, and the boundary layer is turbulent. The values of normal-force coefficient and pitching-moment coefficient have been modified to remove the thrust effects (i.e., thrust-induced force and moments in still air). These values were compared with three-dimensional inviscid flow predictions assuming no base-mounted jets. There is good agreement between the three-dimensional inviscid flow force/moment results and wind-tunnel data with JRC for angles of attack up to -9 deg and $p_{0c} = 60$ psi level. This is consistent with the surface-pressure data as shown before.

At a higher angle of attack ($\alpha > 9$ deg) and higher jet chamber pressure, the leeward plane frustum flowfield exhibits boundary-layer separation. Consequently, the three-dimensional inviscid flow approximation becomes invalid. Even at the highest jet pressure level of 278 psi, the interference effects are small ($\sim$7%). Similar results depict Tunnel B data on force/moment coefficient with base-mounted jets firing at the windward plane. In this case the bare-body force/moment aerodynamic coefficients are not affected by the base jets at any angle of attack, even at the highest jet pressure level. This is also consistent with the wall-pressure measurement, which shows the frustum shock layer is not perturbed by the base jets. The high wall pressure on the windward plane prevents the upstream influence of the jet penetration.

Code Validation

For computer code validation purposes a comparison of CFD results with data at $p_{0c} = 60$ psia, Mach 8, and $\alpha = 0$ deg is shown in Figs. 16a–16d. Good agreement between the measured wall pressure and Navier–Stokes prediction is noted.

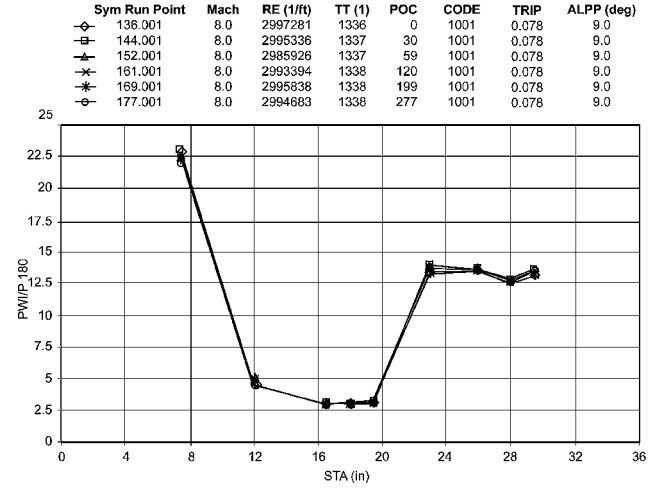

Fig. 14a Wind Tunnel B windward surface-pressure distributions: α = 9 (Reaction jets are fired at windward plane.)

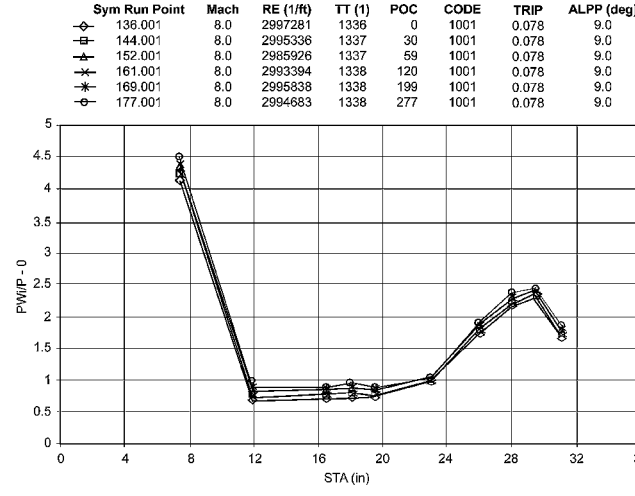

Fig. 14b Wind Tunnel B leeward surface-pressure distributions: $\alpha = -9$ deg. (Reaction jets are fired at windward plane.)

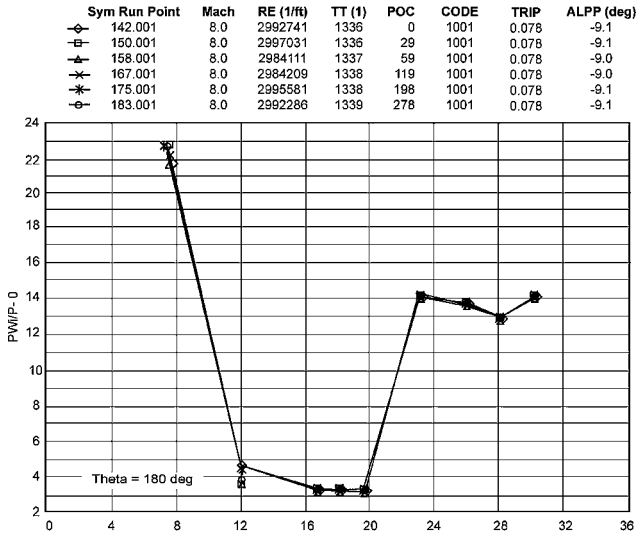

Fig. 14c Wind Tunnel B windward surface-pressure distributions: $\alpha = -9$ deg. (Reaction jets are fired at leeward plane.)

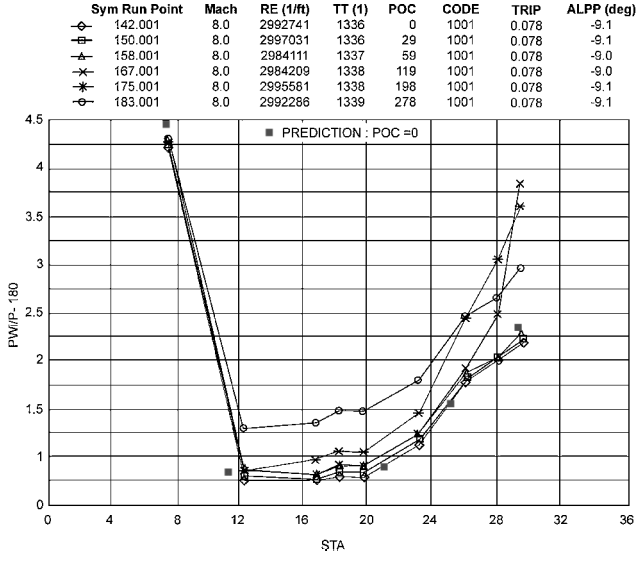

Fig. 14d Wind Tunnel B leeward surface-pressure distributions at $M_\infty = 8$ and $\alpha = -9$ deg showing boundary-layer flow separation at jet stagnation pressures 119, 198, and 278 psia. (Reaction jets are fired at leeward plane.)

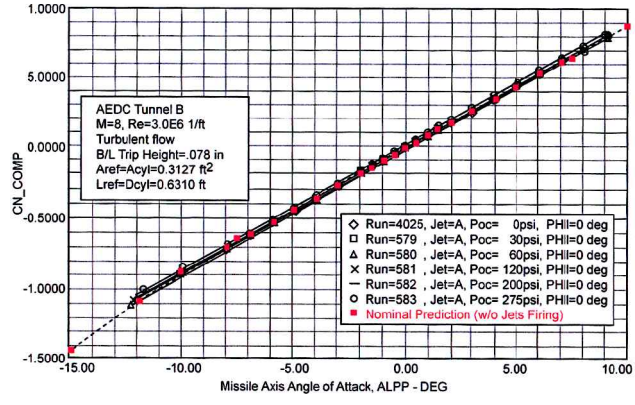

Fig. 15a Normal-force coefficient (thrust component removed).

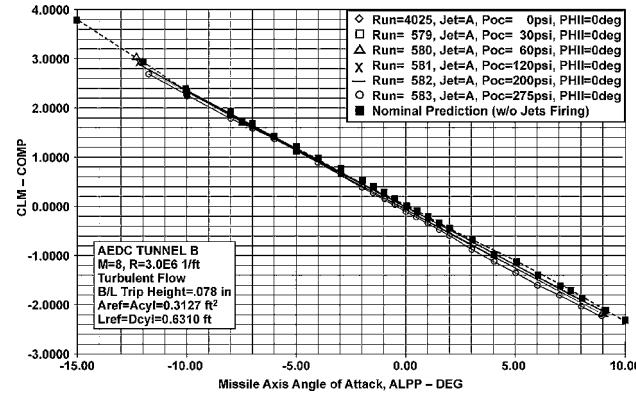

Fig. 15b Pitching-moment coefficient (thrust component removed).

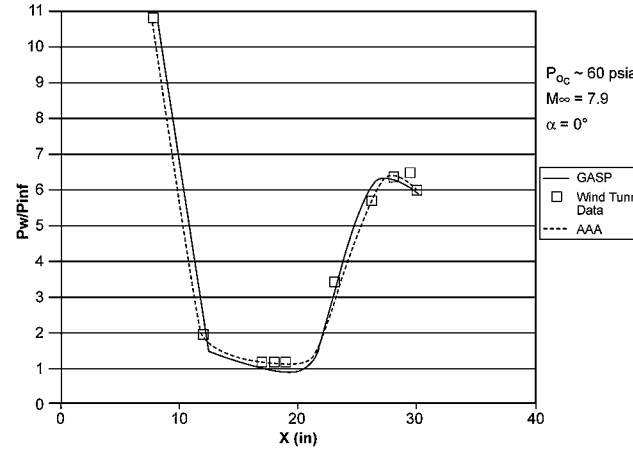

Fig. 16a Comparison of AEDC Tunnel B data with CFD (GASP) predictions.

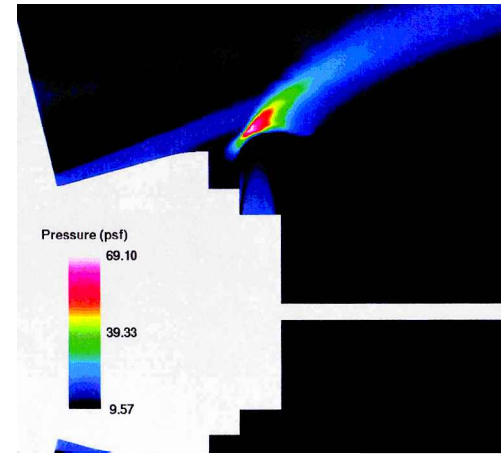

Fig. 16b Predicted pressure contour near RV base region ($M_\infty = 8$ and $\alpha = 0$ deg.

The next case considered was for the TsRV flying at angle of attack of 9 deg and the base- mounted JRC firing at the windward plane. Figure 17 presents the calculated surface-pressure distribution from three-dimensional inviscid flow code[5] at the windward plane and compares it with with AEDC data. In this case, the frustum flowfield is not affected by the JRC plume. The inviscid flow predictions compare favorably with the Tunnel B data.

In the case of the JRC firing at the leeward plane of the base region, the surface-pressure predicted by GASP still compares reasonably well with the AEDC data on the windward plane (Fig. 18a) but less satisfactorily at the leeward plane (Fig. 18b). The three-dimensional flowfield indicates that the frustum boundary layer separates at the

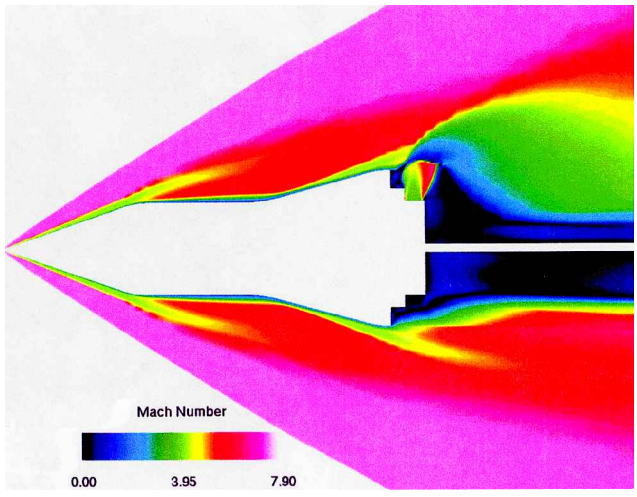

Fig. 16c Predicted Mach contour near RV base region (M_∞ = 8 and α = 0 deg.

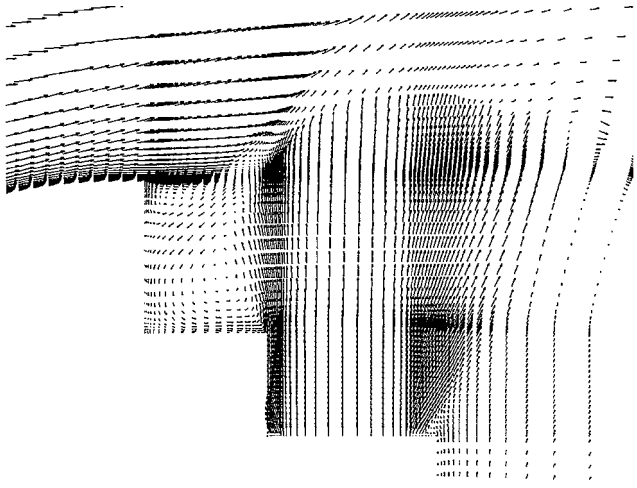

Fig. 16d Predicted flow velocity projection near RV base region: M_∞ = 8 and α = 0 deg. (JRC was fired at the base.)

leeward plane and the separation bubble extends upstream of the flare, that is, the cylindrical section of the body (Fig. 19). Similar observations can be inferred from the AEDC shadowgraphs and the wall-pressure measurements. However, the predicted surface pressure and the Tunnel B data do not agree very well. Additionally, the calculated flowfields exhibited a transient behavior, that is, numerical calculations did not converge to a truly steady solution. Instead, the numerical results indicate that the separation bubble started to slowly pulsate in size, and small oscillations in flow properties (e.g., wall pressure) were noted. A similar type of unsteady boundary-layer separation was found by Wang et al.[9] in their analysis of jet interaction with a supersonic flow.

The cause of the discrepancy between the GASP prediction and Tunnel B data on wall pressure for the case ($\alpha = 9$ deg, jet firing at the leeward plane) involving shock-layer separation is not known at this time. Grid refinements were made in the GASP code (i.e., the mesh points in leeward separated flow regimes were tripled). However, this finer grid did not improve the agreement with the test data. Next, it was postulated that the turbulence model used in the simulation plays a role. To find out, calculations were performed using a k–ε turbulence model. Numerical results did not differ significantly from the Baldwin and Lomax turbulence model results and did not significantly improve the agreement with AEDC Tunnel B data. It was also speculated that the use of boundary-layer trips in AEDC Tunnel B might play a role on the state of the boundary layer. Regardless of this discrepancy, because one major purpose of the wind-tunnel tests and the CFD computations is to estimate the onset of frustum separation caused by the jet interaction, we have achieved our goal.

Finally, AEDC Tunnel A tests were planned to simulate the TsRV aerodynamics at low altitude, where Mach number is low but ambient pressure and Reynolds number are high. As expected, the Tunnel A ($M_\infty = 4$) force/moment data indicated no jet interaction effects, regardless of thrust level or angle of attack (i.e., at the highest jet stagnation pressure and highest angle of attack tested). This is because the $p_{0c}/p_{\text{ambient}}$ is smaller at lower altitudes [see Eq. (2)]. Consequently, the jet penetration or Mach disk is smaller in size at higher ambient pressure environments (i.e., with constant jet chamber pressure).

The aerodynamic coefficients and wall-pressure measurements just discussed show conclusively that base-mounted thrusters can be configured to avoid the significant aerodynamic perturbations that are observed with frustum-mounted jets or windward flaps.

Sym	Run.Point	Mach	RE (1/ft)	TT (1)	POC	CODE	TRIP	ALPP (deg)
◇	139.001	8.0	2992741	1336	0	1001	0.078	-9.1
□	147.001	8.0	2997031	1336	29	1001	0.078	-9.1
△	155.001	8.0	2984111	1337	59	1001	0.078	-9.0
×	164.001	8.0	2984209	1338	119	1001	0.078	-9.0
✳	172.001	8.0	2995581	1338	198	1001	0.078	-9.1
○	180.001	8.0	2992286	1339	277	1001	0.078	-9.1

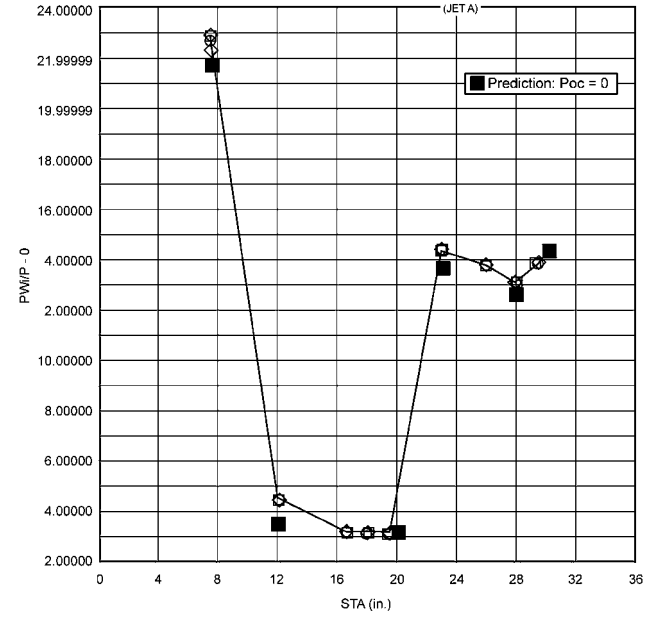

Fig. 17 Wind Tunnel B windward surface-pressure distributions (nondimensionalized with freestream pressure) windward jet at α = 9 deg.

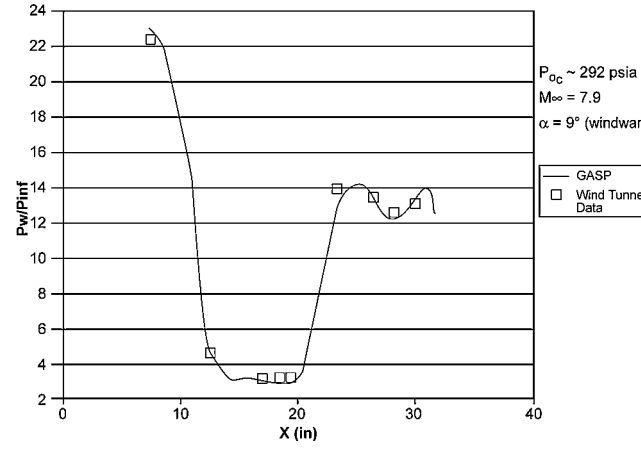

Fig. 18a Comparison of AEDC Tunnel B data with CFD prediction on windward wall pressure: M_∞ = 8 and α = 9 deg. (JRC was fired at leeward plane.)

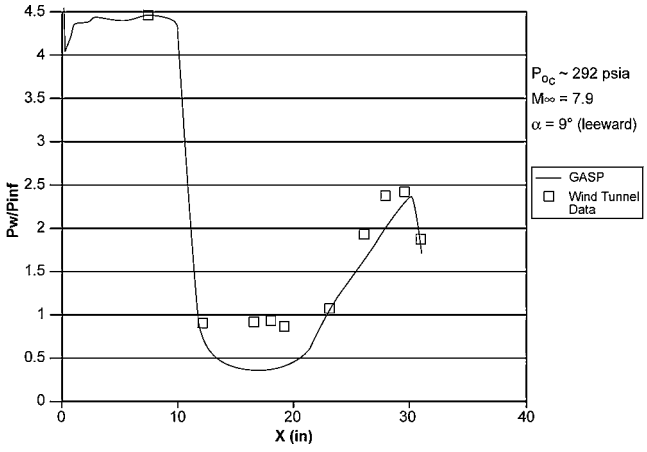

Fig. 18b Comparison of AEDC Tunnel B data with CFD prediction on leeward wall pressure: M_∞ = 8 and α = 9 deg. (JRC was fired at leeward plane.)

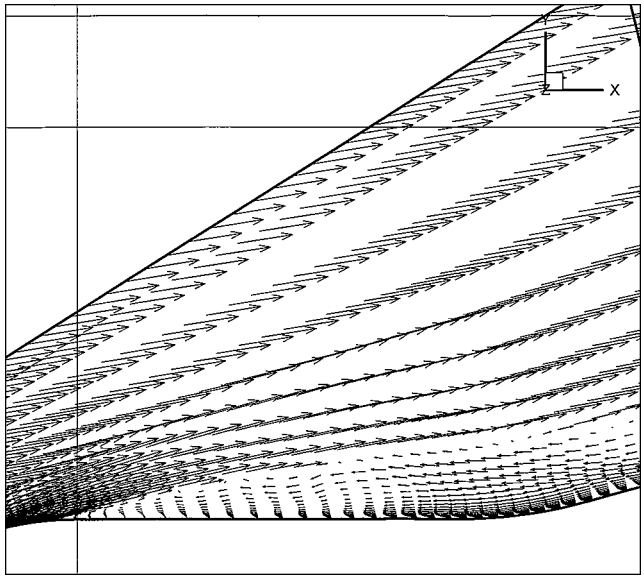

Fig. 19 Velocity vector projection at leeward plane: α = 9 deg and M_∞ = 8. (Jet firing at RV base at leeward meridian.)

Tunnel B ($M_\infty = 8$) results indicate no measurable perturbations in forces/moments for jet stagnation pressures of up to 60 psia at $\alpha < -10$ deg, for JRC firing at the leeward plane. This condition simulates one of the worst-case flight conditions of a particular maneuvering mission ($h = 80$ kft, $\alpha = 10$ deg). Some degree of interaction begins at $\alpha < -10$ deg; however, the aerodynamic coefficient perturbation by leeward thrusters is small at angles of attack up to -14 deg. If a higher angle of attack, or operation at higher jet stagnation pressure is desired, the interaction forces can still be kept to virtually zero by using a windward thruster (see Figs. 2b, 14a, and 14b). In this case the TsRV must operate at a slightly negative margin. The autopilot control algorithms must be designed carefully. Over the years, maneuvering RVs with negative static margins have been designed and flight tested. One has to be sure the TsRV is flying in the design flight regime.

Summary

A new design approach has been proposed for the trajectory-shaping reentry vehicle. Using an axial moving mass to place the TsRV's c.g. at its aerodynamic center of pressure, a very small, base-mounted jet thrust can trim the RV at large angles of attack. As a result, very little jet fuel weight is required. Because the vehicle's static margin can be kept to almost zero, the lifting command reaction time is fast. Also, by properly positioning the jet below the base shoulder of the TsRV plume and shock-layer interaction can be avoided. Consequently, the aerodynamic coefficients of the RV are unaltered by the insertion of base jets (except for a small reduction in axial-force coefficient caused by the jet impingement on the RV base). Usually, the aerodynamic coefficients of the basic conic bodies are well known, and simple inviscid flow CFD tools can predict them. Therefore expensive wind-tunnel tests are not needed for the proposed design. The hardware for jet reaction control can be obtained as commercial-off-the-shelf items. Although the design of a moving mass is by no means simple, it is straightforward and doable.

Extensive Navier–Stokes computations were made to validate the concept of the use of base-mounted JRC to produce large trim angle without causing interference to the missile/RV frustum flowfields. The CFD results were compared with AEDC Tunnel B and Tunnel A data, and reasonably good agreement was found between the tunnel measurements and numerical predictions, up to the point where frustum shock layer is perturbed by the jet interaction.

The basic concept proposed here is demonstrated with an aeroshell of sphere-cone-cylinder-flare configuration (whose lift to drag ratio is of the order of L/D ~ 1.6). Actually, the design approach can be applied to any aerodynamic frame, even for a vehicle with noncircular cross section (where L/D can be relatively large, e.g., L/D ~ 4), or to any control algorithms (skid-to-turn or bank-to-turn).

References

[1]Fote, P., and Thyson, N. A., "Conventional Ballistic Missile Design Manual," Textron System Div., Rept. TSC-272-100047, Wilmington, MA, May 1999.

[2]Crist, S., Sherman, P. M., and Glass, D. R., "Study of Highly Underexpanded Sonic Jets," *AIAA Journal*, Vol. 4, No. 1, 1966, pp. 68–71.

[3]Zukoski, E. E., and Spaid, F. W., "Secondary Injection of Gases into a Supersonic Flow," *AIAA Journal*, Vol. 4, No. 2, 1964, pp. 1689–1696.

[4]Spaid, F. W., and Cassel, L. A., "Aerodynamic Interference Induced by Reaction Controls," AG-173, AGARD, Dec. 1973.

[5]Hall, D. W., and Sontowski, J., "A Three Dimensional Inviscid Flow Field Code for Maneuvering Reentry Vehicles with Non-Circular Cross Section and Flap Control Surfaces," AFSC, BMO-TR-86-06, Valley Forge, PA, Feb. 1986.

[6]McKeel, S. A., Waters, R. W., and Chadwick, K. M., "Investigation into Transition Modeling," *Proceeding of the 12th AIAA Computational Fluid Dynamics Conference*, AIAA, Washington, DC, 1995.

[7]Conti, R. J., "Advanced Aerothermal Algorithm," Hypersonic, Inc., U.S. Air Force Ballistic Missile Office, Rept. BMO-TR-95-25, San Bernardino, CA, Sept. 1995.

[8]Kealos, J., "CBM Wind Tunnel Test Report," Textron System Corp., Rept. TSC-0028-99-CR, Wilmington, MA, June 1999.

[9]Wang, J. C. T., Than, P. T., and Ndefo, E. D., "Transient Flow Field of a Sonic Jet in a Vortical Supersonic Cross Stream," AIAA Paper 95-2374, July 1995.

W. E. Williamson
Associate Editor

Color reproductions courtesy of Northrop Grumman Mission Systems.